Annihilation of action potentials induces electrical coupling between neurons

Moritz Schlötter[1,2*], **Georg Maret**[1], **Christoph J. Kleineidam**[2]

***For correspondence:** moritz.schloetter@uni-konstanz.de (MS)

[1]Department of Physics, University of Konstanz, Germany; [2]Neurobiology, Department of Biology, University of Konstanz, Germany

Abstract Neurons generate and propagate electrical pulses called action potentials which annihilate on arrival at the axon terminal. We measure the extracellular electric field generated by propagating and annihilating action potentials and find that on annihilation, action potentials expel a local discharge. The discharge at the axon terminal generates an inhomogeneous electric field that immediately influences target neurons and thus provokes ephaptic coupling. Our measurements are quantitatively verified by a powerful analytical model which reveals excitation and inhibition in target neurons, depending on position and morphology of the source-target arrangement. Our model is in full agreement with experimental findings on ephaptic coupling at the well-studied Basket cell - Purkinje cell synapse. It is able to predict ephaptic coupling for any other synaptic geometry as illustrated by a few examples.

Introduction

Neurons are characterized by electrically excitable membranes and most neurons in a brain are able to generate action potentials (APs) which are propagating along the axon. At the synaptic terminal they eventually lead to electro-chemical processes, allowing communication with postsynaptic target neurons (***Eccles, 1982***). The most prevalent form of communication between neurons is by transmitter release at the presynaptic terminal, and subsequent binding of these at postsynaptic sites leads to excitation or inhibition. Less common in nervous systems of any organism are gap junctions between neurons, resulting in an aggregated functional unit because internal current is transferred from one neuron to the other neuron. Beside these two forms of communication between neurons, the electrical field itself which is generated at an excited membrane can have an impact on the membrane potential of cells in the vicinity (***Jefferys, 1995***; ***Anastassiou and Koch, 2015***; ***Rebollo et al., 2021***). Rapid changes of the membrane potential, as it occurs when APs are generated, induce electrical fields, that by superposition are also present in neighboring cells. The impact of a single, propagating AP on adjacent neurons is very small, nevertheless, along active, parallel fibers synchronization of APs can occur (***Katz and Schmitt, 1940***). When the term ephaptic interaction was coined by ***Arvanitaki*** (***1942***), she concluded that the blockage of APs is the main source of such effects (hereafter: ephaptic coupling) in nervous systems. Indeed, APs arriving at the synaptic terminal of a neuron annihiliate, thereby generating a more potent electrical field for ephaptic coupling. The functional significance of ephaptic coupling at synaptic terminals is well documented in at least two systems: At the Mauthner cell in teleost fish and at the Purkinje fibers of the cerebellum in vertebrates (***Furukawa and Furshpan, 1963***; ***Blot and Barbour, 2014***). In both systems, APs arriving at the synaptic terminal of the source neuron (e.g. the Basket cell

of the cerebellum) modulate the initiation of an AP in the target neuron by transiently changing the membrane potential. Although the phenomenon of ephaptic coupling is known since many decades (***Arvanitaki, 1942***), a quantitative physical description is missing. This is even more surprising when considering that ephaptic coupling at synaptic terminals is ubiquitous and may well contribute to communication between many different types of neurons, beside the mentioned Mauthner cell and Purkinje fiber. In our study, we aim to describe the electric field of an AP arriving at the synaptic terminal in such detail that the ephaptic coupling and the change in membrane potential of a known target neuron can be predicted.

The propagating action potential is driven by a voltage dependent transition of the membrane from a resting to an excited state. As a consequence of electro-neutrality, current flows across the membrane resulting in a closed loop through extracellular and intracellular medium. The current loop includes the resistive extracellular medium where the AP generates a voltage signature. In 1952, Hodgkin-Huxley introduced a model (HH model) for generation and propagation of APs (***Hodgkin and Huxley, 1952***). It is based on the cable equation and incorporates Nernst equations for different ions and changing ion specific conductances upon activation of ion channels. The HH model is a powerful tool to study and evaluate the properties of ion channels in excitable membranes on a microscopic level, and the great attention it received since being introduced is more than justified (***Catterall et al., 2012***). However, the macroscopic phenomenon of current loops and associated electric fields is already well accounted for by a much simpler model introduced by Tasaki and Matsumoto (***Tasaki and Matsumoto, 2002***; ***Tasaki, 2006***) (TM model) without the need of a multitude of specific parameters as required for example in the HH model. While the TM model can be considered as a simplification of the HH model, the mechanism that the authors had in mind is very different (***Tasaki, 2002***; ***Tasaki et al., 1965***, ***1971***). In general terms, neural membranes can go through transitions where the electric properties change extremely fast (***Fedosejevs and Schneider, 2022***; ***Mussel et al., 2021***; ***Horkay et al., 2000***). The TM model describes a resting and an excited state, each with a linear cable model. It uses the cable equation with two state-specific parameters, its equilibrium potential and conductivity, which undergo a sudden (voltage dependent) switch at the boundary between resting and excited state. The boundary between an excited and a resting section propagates towards the resting side. The AP in the TM model has only 3 degrees of freedom, e.g. its propagation velocity, its amplitude and the length of the AP. Nevertheless, the TM model is well suited to describe the current distribution that is driven by the inhomogeneity of local electric fields in the internal and the external medium. Thus, the TM model possibly already is sufficient to describe the mutual influence of neurons by ephaptic coupling, using only three parameters for each neuron.

It is therefore of prime importance to evaluate the quantitative description of the TM model based on experimentally derived values. We explore the behaviour of APs at boundaries to assess these three parameters. A suitable boundary condition can be generated experimentally by a collision of two counter-propagating APs (***Tasaki, 1949***; ***Spach Madison S. et al., 1971***; ***Shrivastava et al., 2018***; ***Shrivastava, 2018***). Within any cable model, the very same boundary condition also exists at the reflecting synaptic terminal of a neuron due to the broken translation symmetry for the current loops (***Spach and Kootsey, 1985***).

In this study, we first focus on collisions of APs. Our experimental observation of colliding APs provides unique access to the spatial profile of the extracellular potential around APs that are blocked by collisions and thus annihilate. Our procedure is as follows: Recording propagating APs allows to determine both the propagation velocity and the amplitude of the extracellular electric potentials. The collision experiment provides additional information on the characteristic length $\lambda^\star$, thereby fully determining the parameters of the TM model. We find that TM is sufficient to describe the onset of the electric field dynamics of an AP. However, as TM does not include the slow return of the excited membrane to the resting state we introduce an extension of the TM model that we call the Relaxing Tasaki Model (RTM) which adds an empirical slow relaxation term to the TM model. We find that RTM accounts for the full spatio-temporal signature of propagat-

ing and colliding APs and is therefore also very useful to predict electric effects at axon terminals e.g. at synapses. Since the RTM model sets a complete framework to describe APs and to predict ephaptic interactions for a given morphology, the RTM model is used in the last part of this paper to simulate various representative pre- and postsynaptic morphologies and geometries. Around AP propagation boundaries, we find excitatory as well as inhibitory regions, depending on timing, relative position, orientation and morphology of source and target neuron. We expect these predictions to be robust, because the model is absolutely minimal and matches the experimental observations.

Results

Extracellular potential around AP collisions

We record the extracellular electric potential of APs, generated by the median giant fibers (MGF) of the ventral nerve chord of an earthworm using the setup shown in ***Figure 1***A. In a first experiment the ends are stimulated individually and the APs are detected at several positions along the fiber. We verify the vitality of a nerve chord by asserting that both fibers (MGF and the lateral giant fibers (LGF)) reliably conduct APs in both directions, and in our experiments, we investigate selectively the MGF only. The signatures $V_e(t)$ of both orthodromic and antidromic propagating APs look indeed very similar. We observe a biphasic voltage spike propagating with $14.5(11)\,\mathrm{m/s}$ (***Figure 1***B).

In the main experiment, both ends are stimulated simultaneously and the APs collide close to the central recording electrode. We observe that the APs do not penetrate each other but always annihilate at the collision site (***Figure 1***B) (***Tasaki, 1949***). At this position, the trace of $V_e(t)$ becomes more monophasic, with an almost doubled positive peak amplitude (***Figure 1***B). The negative phase of $V_e(t)$ at the collision site is considerably diminished and shows a distinct slow relaxation. The peak amplitude of propagating APs is $2.9(2)\,\mathrm{mV}$ while the colliding APs peak is $5.2(3)\,\mathrm{mV}$.

The width of the collision is a measure of the characteristic length $\lambda^\star$ of the AP and is uniquely revealed by a collision sweep experiment. We experimentally positioned the site of collision along the neuron by introducing a delay between the opposing stimuli. Assuming symmetric propagation velocities, a delay Δt displaces the collision by $x = v_p \Delta t/2$ where v_p is the propagation velocity and x is the distance between the collision and the recording electrode. The spatial extend of the collision process is then found by repeating the experiment at various delays Δt between the opposing stimuli, see (***Figure 1***C). The propagation velocity is derived from the time of arrival at separate recording sites. The peak amplification can be used as a measure of the width of the collision (***Figure 1***D). We use four recordings at three positions (anterior, medial and posterior) along the nerve chord and we assess the mean full width at half maximum as $3.8(5)\,\mathrm{mm}$.

Model of the action potential

We describe a neuron by a classical cable model as shown in ***Figure 2***A (see "Methods" for further details). Such a model consists of a chain of RC circuits composed of resistors with conductivity g_m ($\mathrm{S/m}$) and capacitors c_m ($\mathrm{F/m}$) which are connected by an inner resistivity r_i (Ω/m). The inner axial current I_{ax} is driven by the gradient of the potential $V(x,t)$ inside the neuron. A common approach is to assume a constant capacity and to neglect external fields and inhomogeneities in the neuron. Then, the balance of currents results in the cable equation with the membrane potential V_m

$$\frac{\partial^2 V_m}{\partial x^2} = r_i c_m \frac{\mathrm{d}V_m}{\mathrm{d}t} + r_i g_m V_m \tag{1}$$

The first term on the right describes the capacitive charging by an axial current which is linked to the rate of change in membrane potential. The second term describes the contribution of resistive membrane current to axial current.

APs are characterized by a solitary i.e. non-spreading spatio-temporal shape. In the cable model, the generation of such APs requires an additional non-linear response of the membrane. Commonly, living cells are electrically charged to a negative equilibrium potential V_{eq} across their

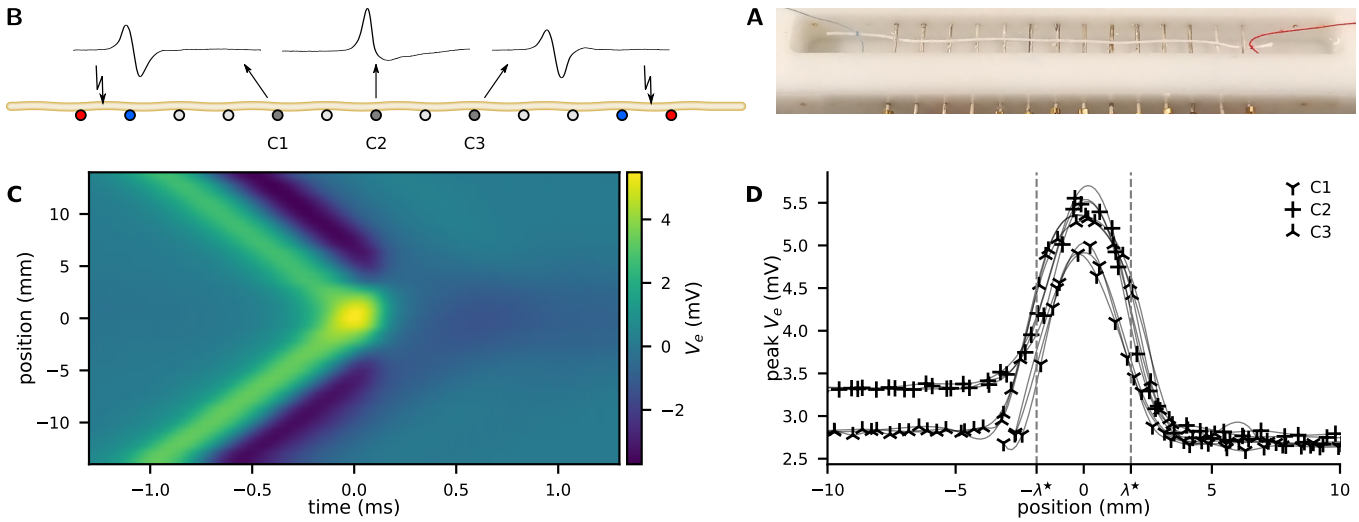

Figure 1. AP collision experiment. **(A)** The ventral nerve chord (VNC) of an earthworm is positioned on a series of transverse, single-ended electrodes to excite and monitor APs. **(B)** Individual or two counter-propagating APs are generated by stimulating the nerve at the outermost electrodes. Some of the inner electrodes (C1, C2, C3) are used for recording, all other electrodes are grounded. Propagating APs generate biphasic electrical potential as sketched above C1 and C3 whereas colliding APs provoke an essentially unipolar peak (cf. C2). By variation of the delay between the opposing stimuli, the collision can be generated anywhere along the nerve between the stimulation electrodes. **(C)** Extracellular recording of propagating and colliding APs. A collision sweep experiment yields multiple recordings with varying distance between recording site and point of collision. The recording of a collision corresponds to the horizontal line in the middle, while orthodromic propagation is at the top and antidromic propagation is at the bottom. The recording was at a medial position. **(D)** The peak amplitude as a function of the distance to the collision. Examples of four recordings at three positions (C1, anterior; C2, medial; C3, posterior) along the nerve chord. As a guide to the eye, the data points are connected by a cubic spline (thin lines).

Figure 1—figure supplement 1. Raw Data

Figure 1—figure supplement 2. Fit of the collision width

membrane. In excitable cells, e.g. neurons, a change of the membrane potential beyond a critical threshold value leads to a rapid transition from the resting into an excited state of the membrane which essentially differ in their respective resistivities. The excited state, with drastically increased conductivity, is indicated by the starred values $g_m^\star$ and potential $V_{eq}^\star$.

A local transition of a membrane from the resting to excited state results in a boundary between $V_{eq}^\star$ and V_{eq}. The difference in membrane potentials between the resting and excited state induces an internal axial current. The increased conductivity at the excited state *drives* the internal current and depolarizes the adjacent membrane. The flow lines of internal, transmembrane and external current form a closed loop around the position of the transition as sketched in ***Figure 2***B. All internal current is present as an extracellular return current and in neurons, this process produces a propagating, dipolar local current source.

The Tasaki-Matsumoto (TM) model describes both the resting and the active state by linear cable models (***Tasaki and Matsumoto, 2002***; ***Tasaki, 2006***). The resting state has a negative electrochemical equilibrium potential $V_{eq} = -100\,\mathrm{mV}$ and a very low conductivity g_m. In the excited state the conductivity is drastically increased to $g_m^\star \approx 100\,g_m$ and the equilibrium potential $V_{eq}^\star$ is zero. The transition from the resting to the excited state is discontinuous and occurs at $V_m = -50\,\mathrm{mV}$. The TM model does not address how the resting state is maintained before a transition, nor does it address how the resting state is restored thereafter.

A simple analytical solution of the TM model describes the propagating initial depolarization of a nerve signal. This includes an exact expression for the propagation velocity v_p, and for the spatial length $\lambda^\star$ of the initial current dipole as illustrated in ***Figure 2***B. The velocity is determined by the delay in charging of neighboring capacitors, while the leak conductivity barely effects the process. Therefore, we base our study on simplified expressions by neglecting the leak conductivity, as it amounts to less than 1% of the conductivity in the excited state (***Tasaki and Matsumoto, 2002***).

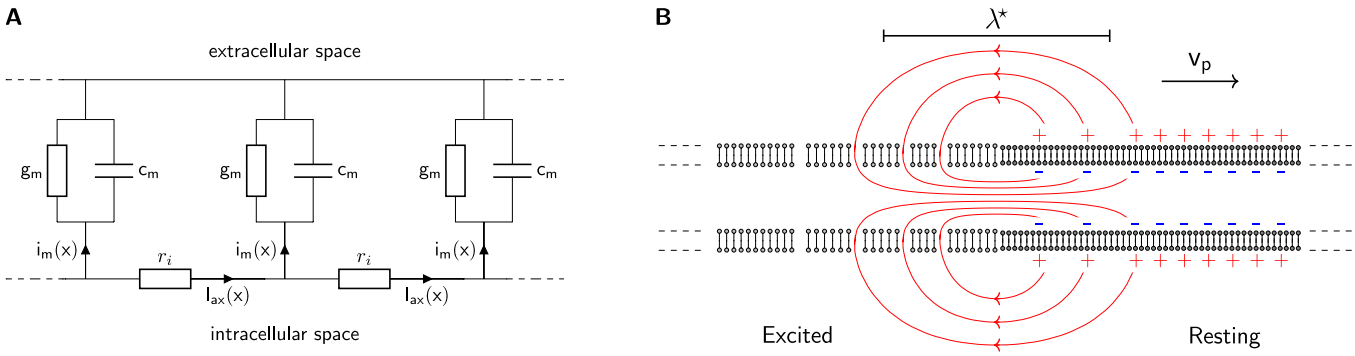

Figure 2. The classical cable model. **(A)** A chain of identical RC circuits with conductivity g_m, capacity c_m and inner resistivity r_i mimics the electric properties of the cellular membrane and connects the extracellular and intracellular space. The change of inner axial current $I_{ax}(x)$ is given by the transmembrane current density $i_m(x)$ (Kirchhoff's current law). **(B)** The propagating solution of the Tasaki-Matsumoto model. A boundary between a resting state and an excited state induces an axial current, that causes a propagation of the boundary. The axial current flows in closed loops and returns within the resistive extracellular medium, causing an extracellular potential that travels with the current source along the neuron.

Then the analytical solution of the TM model yields

$$v_p = \frac{1}{c_m}\sqrt{\frac{g_m^\star}{2\,r_i}} \qquad \text{and} \qquad \lambda^\star = \frac{1}{\sqrt{r_i\,g_m^\star}} \tag{2}$$

Note that the length scale λ^* used here is not equivalent to λ used in basically all previous models where λ denotes the damping length due ionic leakage neglected here. The products in eq. 1 can be expressed as $r_i\,c_m = \left(v_p\lambda^\star\right)^{-1}$ and $r_i\,g_m^\star = \lambda^{\star\,-2}$. According to eq. 1 $(r_i\,c_m)^{-1}$ is the diffusion constant of the spreading potential V_m which connects a typical time scale τ_L with a typical diffusion length L by $\tau_L = r_i\,c_m L^2$. The two products $r_i\,c_m$ and $r_i\,g_m^\star$ are directly determined in our experiment from measurements of v_p and $\lambda^\star$, and for a comparison of our AP measurements with the TM model only one degree of freedom is missing, which is the amplitude of the AP. At this point we fit the amplitude of the model to our experimental recording by estimating an appropriate extracellular conductivity.

The fast switch from resting to excited state in the generation of an AP is followed by a slow process of repolarization that restores the resting state. In order to provide a more general model that also accounts for repolarization we add a simple extension to the TM model and refer to this as Relaxing Tasaki Model (RTM). We approximate the repolarization in the extracellular potential by extending the TM model with an (ad-hock) exponential repolarization function (see "Methods").

Comparison of measurements with model simulations

The above collision sweep experiment provides a detailed survey of the extracellular electric signature of APs. We now compare these results to the TM model, the RTM model and the classical HH model (see "Methods") by simulating a nerve of length 10 cm with 2000 compartments (Conductivities in the HH model are area specific, here we use a diameter of 80 µm). All models are adjusted to the MGF with identical procedure. The parameters r_i and c_m are used to match the propagation velocity v_p and the width $\lambda^\star$ of the collision to the experimentally determined values. The fitting procedure is as follows: (i) Propagating APs are simulated. For a given r_i the velocity is adjusted using c_m. (ii) An AP collision is simulated and the width is compared to the experiment (see ***Figure 1—figure Supplement 2***). If the width deviation is below 1%, the model is accepted. Otherwise r_i is updated and the procedure is repeated from step (i). The TM model obeys the analytical expressions and converges immediately. The RTM model deviates from the TM expressions only by a few percent and converges very fast. The HH model takes more iterations to converge. In all cases, the procedure is unambiguous and stable. The complete parameters for all models are given in ***Appendix 2 — Table 2***.

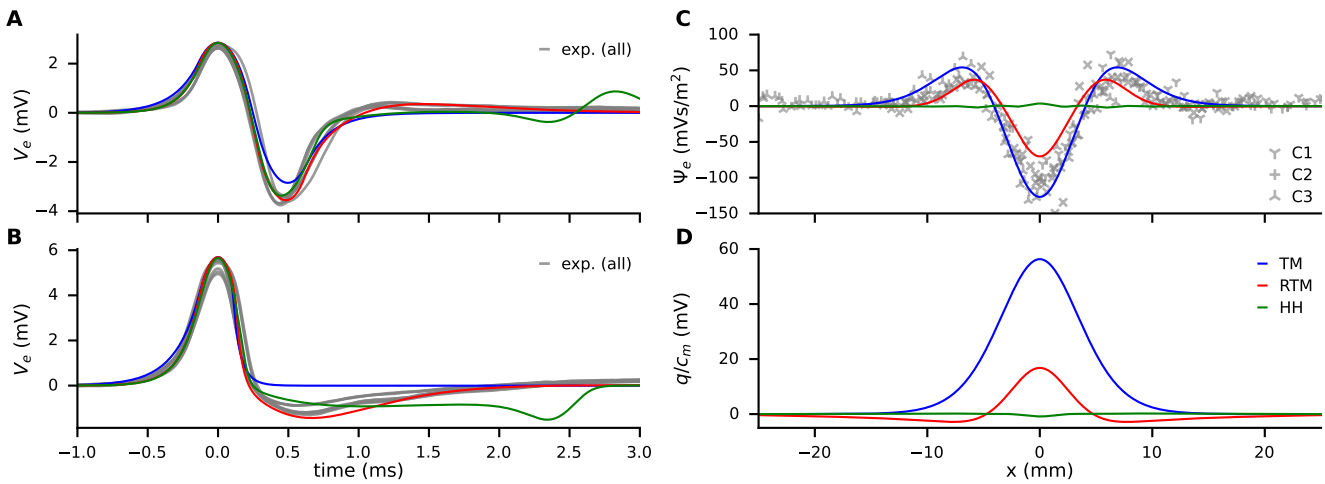

Figure 3. Comparison of experimental data (gray) with models (color, see legend). **(A)** Traces of $V_e(t)$ from propagating APs. **(B)** Traces of $V_e(t)$ at the collision site. **(C)** The extracellular discharge of annihilating APs, measured and calculated. The gray crosses are the experimental values from 4 recordings at 3 separate sites along the MGF, where each recording consists of up to 46 traces with varying delay times. **(D)** Different predictions about the discharge generated by AP annihilation and released around the collision site.

While the individual values of r_i and c_m depend on the choice of $g^\star$, the product $r_i c_m$ does not. From our measurements we obtain $r_i c_m = 26\,\mathrm{s/m^2}$, which is in good agreement with literature values (***Tasaki and Matsumoto, 2002***; ***Tasaki, 2012***). The resulting length parameter is $\lambda^\star = 1.8\,\mathrm{mm}$ which is about half the width of the peak in ***Figure 1***D. The deviations between the TM model and the experiment are: 1. Propagating APs cause a negative peak greater than the positive peak (***Figure 3***A). 2. There is a small but sustained negative phase at the collision site (***Figure 3***B). The repolarization time in the RTM model is found by comparing the model to the experimental traces of the colliding AP (***Figure 3***B). A value of $\tau_r = 0.5\,\mathrm{ms}$ provides an acceptable fit. All models allow the reconstruction of the extracellular field of propagating APs within satisfying accuracy.

Discharge of colliding APs

In an active axon, current always flows in and out in equal amounts (electroneutrality) (***Barbour, 2020***). As long as APs propagate the current must sum up to zero in space at any time and in time at any position. However, when APs are blocked the local sum in time can deviate from zero while the spatial sum remains zero. Annihilating APs generate an effective net charge expelled into the extracellular space and the associated current pulse may act like a stimulating electrode. The transmembrane current i_m is driven by the curvature of the potential $\partial_x^2 V_m$. The total charge expelled along the axon is

$$q(x) = \int \mathrm{d}t\, i_m(x,t) = \frac{1}{r_i} \int \mathrm{d}t\, \partial_x^2 V_m(x,t) \tag{3}$$

where we define the discharge $q(x)$. The three models make very different predictions about the discharge at the collision site (***Figure 3***D). The discharge $q(x)$ is not accessed directly in our measurement, but it is proportional to the residual extracellular curvature

$$\Psi_e(x) = \int \mathrm{d}t\, \partial_x^2 V_e(x,t) \tag{4}$$

that we measure in our experiment. ***Figure 3***C illustrates that the TM model is in excellent agreement with the experiment and the RTM model only slightly underestimates the discharge. From this observation we conclude that the discharge is driven by the rapid onset of the AP and that the contribution by the repolarizing phase is small. On the other hand, the HH model largely disagrees with the experiments both in the magnitude of the discharge and in its temporal shape.

Model of ephaptic coupling

First, we briefly investigate the effects of propagating APs on neighboring parallel cells which may give rise to synchronization (***Katz and Schmitt, 1940***; ***Kriebel et al., 1969***; ***Goldwyn and Rinzel, 2016***). Then, we focus on synaptic terminals i.e. situations where the (finite) electric discharge of *annihilating* APs may influence surrounding target neurons. We showed above that colliding APs emit a charge $q(x)$ and can act like a stimulating electrode. For reasons of symmetry there is no axial current at the point of collision. Within any cable model this is identical to a closed end, thus, it also applies to axon terminals and the synapse (***Plonsey, 1977***; ***Spach and Kootsey, 1985***; ***Kléber and Rudy, 2004***). Knowledge of the generated inhomogeneity of V_e allows to calculate the response of a target neuron that may be close to a site of AP annihilation. The details of this calculation are provided in the methods section. Briefly, the above defined discharge from annihilation at terminals or collisions generates a distortion of the extracellular potential V_e which in turn induces current in nearby target neurons.

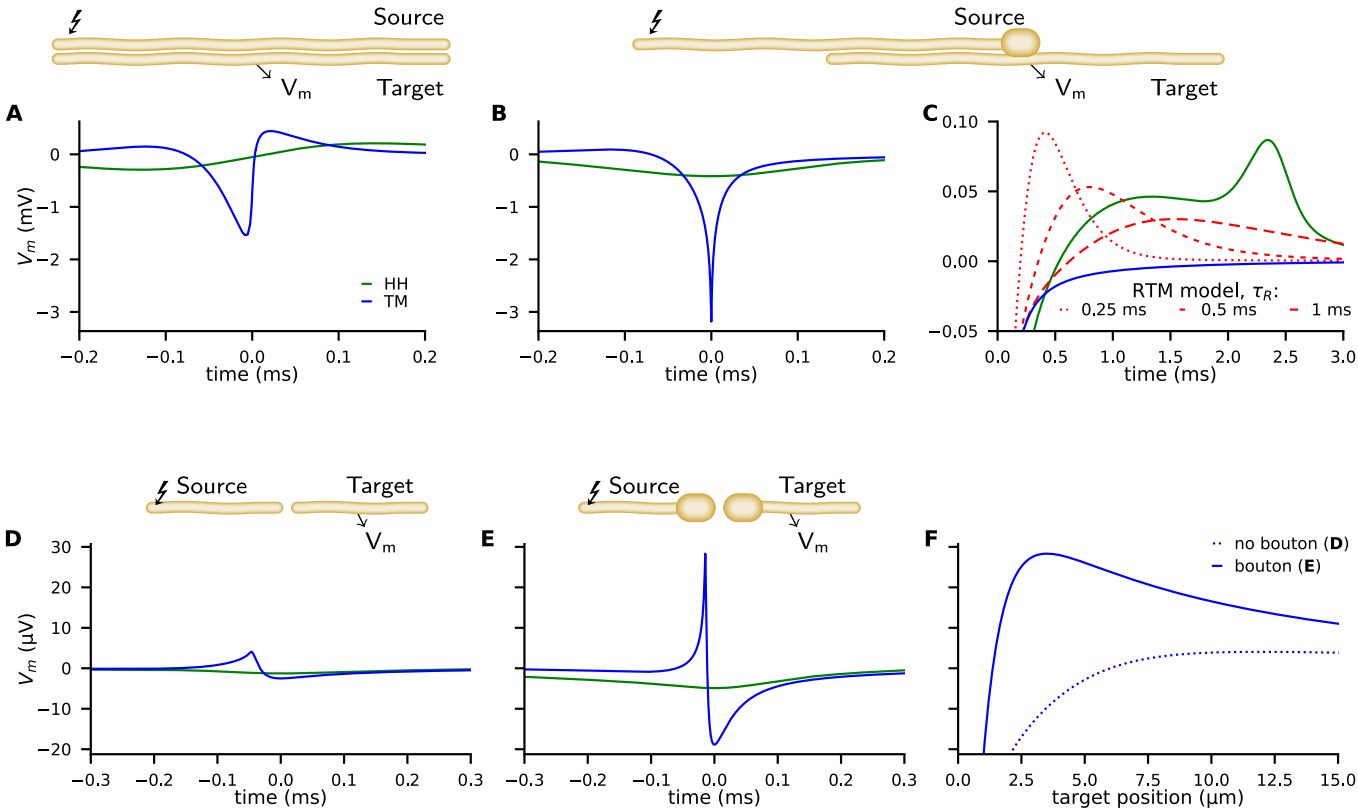

Figure 4. Examples of ephaptic coupling, calculated with the TM-model (blue) and the HH-model (green): **(A)** in a parallel target neuron when an AP is propagating in the source. **(B,C)** when the AP is annihilating (end-to-shaft geometry, similar to the Basket cell–Purkinje cell synapse). The source and target neurons are $1\,\mu m$ in diameter and are separated by $1\,\mu m$ (2000 compartments each, length $1\,mm$, bouton size $2\,\mu m$. The neurons are placed next to each other, that is to say the numeric point compartments are separated by $1\,\mu m$. Traces denote the target membrane potential next to the point of axon termination. The initial hyperpolarization effect may be followed by a subsequent depolarization, depicted by the RTM model (red) for different relaxation times. **(D-F)** Ephaptic coupling in an end-to-end synapse, illustrating the enhanced ephaptic coupling, due to enlarged neuron terminals (boutons). Here the source and target neurons are 100 nm in diameter (2000 compartments each, length $300\,\mu m$, bouton size $400\,nm$). The target neurons are 1/4 in length and N (500 compartments, length $75\,\mu m$). The TM model generates a distant depolarization. Traces in D and E show the membrane potential of the target at the point where the TM model provokes its maximal depolarization (corresponding to the peaks in F). Traces in F show the spatial profile of the membrane potential along the target, at the time of maximal depolarization (corresponding to the peaks in D, E).

Figure 4—figure supplement 1. More details of the end-shaft synapse simulation

Figure 4—figure supplement 2. More details of the end-end synapse simulation

In ***Figure 4*** we show simulations of ephaptic coupling in three different geometries: parallel

neurons, end-shaft synapses and end-end synapses. We use common literature values (extracellular resistivity $\rho_e = 100\,\Omega\,\mathrm{m}$ (***Weiss et al., 2008***), inner resistivity $\rho_i = 1\,\Omega\,\mathrm{m}$, membrane capacity $c_m = 10\,\mathrm{mF/m^2}$). The peak membrane conductivity in the TM and RTM models is $g^\star = 450\,\mathrm{S/m^2}$, and the HH model is used with all classical parameters as specified in the supplementary material (e.g. $\bar{g}_{Na} = 1200\,\mathrm{S/m^2}$). ***Figure 4***A shows the potential $V_m(t)$ of the target neuron at the position marked by an arrow when excitation of a propagating AP occurs in the source neuron above. While the response in the target neuron calculated by the HH model is weak and broad, it is more asymmetric, peaked, shorter and stronger in the TM model. Next, we consider an axon terminal that ends near to a neighboring, parallel target fiber. The chosen geometry as sketched in ***Figure 4***B is a coarse representation of the synapse between Basket cell and Purkinje cell with the synapse embedded in a highly resistive structure, called the pinceau (or basket) at the axon initial segment (AIS). The TM and RTM model predict a strong and sharp initial hyperpolarization of the target neuron while the HH model predicts a comparably weak and smooth effect (***Figure 4***B, see also ***Figure 4—figure Supplement 1***). In the RTM and HH models, this initial effect is followed by a more or less pronounced slow depolarization of the target neuron (***Figure 4***C). The RTM model also reveals that a faster repolarization of the source AP increases the late depolarization of the target neuron.

To highlight the relevance of morphology and geometry, we consider target neurons pointing towards the site of annihilation (***Figure 4*** D-F, see also ***Figure 4—figure Supplement 2***). The geometry is reminiscent of an excitatory synapse, where an axon terminal is facing towards a dendritic spine. We choose the same parameters that we used for the end-shaft synapse, but the target neuron is placed in projection of the source nerve with a gap in between them of $10\,\mathrm{nm}$. We include enlargements at the ends since boutons are common at the source and target neuron. Such enlargements significantly amplify ephaptic coupling. We observe that the strong hyperpolarization of nearby postsynaptic membranes is accompanied by a distant depolarization. In ***Figure 4*** D,E we present the time course of the induced membrane potential in the target at the point of maximal depolarization. In ***Figure 4*** F the spatial profile of the induced voltage is given at different times.

The total amplitude of ephaptic coupling strongly depends on the choice of parameters. If we use $g^\star = 1200\,\mathrm{S/m^2}$ (as commonly used in the HH model) instead of the $450\,\mathrm{S/m^2}$ used in ***Figure 4***, the effect more than doubles. Note that much higher values up to $30\,\mathrm{kS/m^2}$ have been reported for specific locations (***Holt and Koch, 1999***) which suggests even stronger ephaptic interactions in certain situations. The distant depolarization shown for the end-end synapse (***Figure 4*** D,E) is only a few tens $\mu\mathrm{V}$, but as the amplitude of synchronized input from many dendrites adds up and cerebellar neurons have thousands of dendrites we may expect depolarisation signal strengths in the mV range.

Discussion

Our experimental design of a custom made recording chamber with a nerve, hanging over a series of electrodes allows accurate measurements of the space and time dependent extracellular field V_e. Since, according to eqs. 9, variations of V_e mirror variations of the membrane current i_m, we obtain information on i_m, on the associated velocity v_p and length scale $\lambda^\star$ of APs. Both of them are measured with great accuracy (about 10%), which allows us critical bench-marking of current theoretical models of AP´s. We find that both, the Tasaki-Matsumoto model and the Hodgkin-Huxley model are well suited to describe the extracellular electric potential of propagating APs which have symmetric forward and backward flow of i_m.

However, when an AP encounters a boundary, either at a axon terminal or in a collision with a counter-propagating AP, the current flow and V_e become asymmetric. In fact, AP propagation is terminated when the overall local axial current is annihilated by a reflection or collision event. At this point, the lack of internal stimulating current causes APs to disappear, as already described by ***Tasaki*** (***1949***). During AP annihilation, the extracellular potential becomes a distinct monophasic spike. This phenomenon has been observed for artificially produced as well as naturally occurring collisions in various systems (***Spach Madison S. et al., 1971***; ***Steinhaus et al., 1985***; ***Tasaki, 1949***,

1955). We quantify the annihilation process by the time integrated charge q (eq. 3) which differs from zero. From collision experiments with finely varying delays between counter-propagating pulses, we extract the spatial shape of the discharge parameter ψ (eq. 4). We find that the experimentally observed discharge is predicted very well by the TM/RTM models, while it is drastically underestimated by the HH model. The excellent fit of the TM model suggests that the discharge of annihilating APs is predominantly driven by the rapid depolarization at the onset of AP generation. The failure of HH is in line with observations made in various studies, indicating that the rapidity of membrane dynamics is not well described by the HH model (***Cole and Moore, 1960***; ***Baranauskas and Martina, 2006***; ***Naundorf et al., 2006***).

Our quantitative physical description of ephaptic coupling between neurons provides a theoretical framework for investigating biological systems in which the phenomenon of ephaptic coupling already has been described and to explore other neural connections. The general cable equation, linking field inhomogeneity to membrane current, applies to both source and target cell. This leads to a coupling between source and target, driven by the electric field and its inhomogeneities. The cable model directly explains why AP-induced membrane current in a neuron induces membrane current in targets (***Durand, 2014***; ***Merrill et al., 2005***; ***Tung, 2021***). Surprisingly, this straight forward concept has never been applied to ephaptic coupling at synapses. Virtually all numerical computations of ephaptic coupling rely on the HH model which, as shown above, is not suitable to predict the effects caused by AP annihilation.

Electrical fields of propagating APs create positive and negative currents in equal amounts and a propagating AP first hyperpolarizes, then depolarizes a parallel aligned target neuron. This may cause synchronization of APs and our proposed model also can be used to study the observed phenomena of synchronization due to ephaptic coupling, even in the case of zero discharge (see ***Figure 4***A).

In contrast, AP annihilation in the source neuron acts as a strong local current injection. The non-zero discharge causes a more pronounced ephaptic coupling effect. AP annihilation occurs at the axon terminal and we have investigated ephaptic coupling for two neural connections to a greater extent. Both, the pre- and postsynaptic neurons have similar morphology and orientation and in addition, accessory structures at the site of connection. In teleost fish, an interneuron with an axon cap can have inhibitory, ephaptic coupling on the Mauthner cell's axon initial segment (AIS) where APs are initiated (***Korn and Faber, 1975***, ***2005***).

In the vertebrate cerebellum, the Basket cells show ephaptic coupling with the Purkinje cell, and, comparably to the Mauthner cell, the generation of APs at the AIS is inhibited by a fast gating mechanism. In the following, we use the Basket cell – Purkinje cell connection as reference and for comparison to our model(s). As in all spiking neurons, an AP in the Basket cell generates a positive extracellular potential, and it is well documented that the Purkinje cell is very sensitive to extracellular potentials, since already $200\,\mu\mathrm{V}$ modulates its firing rate (***Blot and Barbour, 2014***). The cap structure (pinceau or basket (***Ramón y Cajal, 1909***)) around the terminal of the Basket cell restricts local currents to the Purkinje cell, increasing its sensitivity at the AIS to extracellular potentials (***Blot and Barbour, 2014***). The TM model predicts a fast and strong inhibition when APs are annihilating at the Basket cell (***Figure 4***B). Our numerical simulation revealed that in addition to the inhibitory effect of an annihilating AP at onset, a delayed ($0.5\,\mathrm{ms}$ to $1.5\,\mathrm{ms}$ later) depolarization can occur at the target neuron. The magnitude of this depolarization depends on the time course of AP repolarization at the source (***Figure 4***C). Presynaptic variation of AP width is a widespread mechanism for modulation of synaptic transmission by changing transmitter release, and ephaptic coupling possibly contributes to a direct modulation at the postsynaptic neuron (***Begum et al., 2016***; ***Southan and Robertson, 1998***; ***Kole et al., 2015***). ***Blot and Barbour*** (***2014***) described a biphasic modulation of Purkinje cells with delayed and synchronized APs in Purkinje cells after ephaptic inhibition by the Basket cells. In their study, the drug GABAzine was used to investigate the controversially discussed role of GABA for this modulation (***Iwakura et al., 2012***). However, a biphasic modulation is consistent with the purely electrical framework provided in our RTM model, and it remains to be

investigated whether presynaptic modulation of AP width is the underlying mechanism for modulating the biphasic ephaptic coupling of Purkinje cells.

Our finding and formal description of the strong ephaptic coupling generated by annihilating APs impose the need and provides the possibility to examine bioelectric effects in other areas. Endogenous electric fields can influence molecular processes within cells, leading to cell growth, maturation, migration and regeneration(***McCaig et al., 2000***; ***Levin et al., 2017***; ***Funk, 2015***; ***Lyckman and Bittner, 1992***). The orientation of molecules and resulting structures can be induced by homogeneous electric fields and dielectric molecules can accumulate in field inhomogenities by dielectrophoresis (***Cifra, 2012***; ***Pokorný, 2001***). In principle such effects can lead to persistent structural changes in neurons and thus may contribute to neural plasticity and memory. During synapse formation, presynaptic neurons interact with spines of the prospective postsynapse. Prior, or in parallel to chemical communication between the neurons that subsequently will form a synapse, Hebb's rule might be implemented by a discharge from the source and coincident activity in the target. In this case, ephaptic coupling might be instructive for synapse formation. We included calculations on ephaptic coupling with the geometry of an end-to-end synapse and boutons on source/target (***Figure 4*** C-E) and we find that there is an initial sharp depolarization, followed by a slight hyperpolarization. Ephaptic coupling is highly amplified when source and target neurons have boutons, and such a morphology is omnipresent in spines and also presynaptic terminals commonly have enlargements as well. It is important to highlight the importance of source–target geometry, predicted by our TM/RTM models, with opposite effects of ephaptic coupling in the two configurations: end-to-shaft and end-to-end. Our calculation further makes clear predictions where at the target (spine) depolarization can be expected, and this is the case about 1 μm away from the very tip of the target.

Besides the annihilation of APs at the axon terminal, bidirectional propagation and hence collisions of APs might be more common than previously assumed (***Mateus et al., 2021***; ***Scott et al., 2007***; ***Debanne et al., 2011***). In theory, collisions can be used to perform computations (***Siccardi et al., 2016***) and neural networks possibly also perform such kind of information processing. For example, neurons for sound source localization perform a timing analysis based on binaural input. A neural network described as Jeffress delay line can accomplish such computation (***Jeffress, 1948***). ***Franken et al.*** (***2021***) performed a delay sweep experiment and their findings on integration at MSO neurons (Medial Superior Olive neurons in vertebrates) look intriguingly similar to our collision experiment. Time differences and coincidence, in this case, is mapped on a location, e.g. the point of collision where a discharge with a center-surround profile is generated (***Figure 3***C) (***Treue, 2014***).

Irrespective of such speculative functionalities, ephaptic coupling is ubiquitous. Its effects span spectacular length and time scales, in some cases it can bridge up to hundreds of microns (***Kriebel, 1968***; ***Chiang et al., 2019***; ***Shivacharan et al., 2019***). Our formal description of ephaptic coupling between neurons provides a framework to study the functional significance of electric fields as a general mechanism for information processing in neural networks.

Methods and Materials

Experimental design

The objectives of the study were (i) to measure the electric field around propagating and colliding APs with unprecedented accuracy; (ii) to benchmark a powerful yet simple model of APs; (iii) apply this model to demonstrate its predictive power for ephaptic coupling in general.

Sample preparation

The experiments were performed with the ventral nerve chord (VNC) of earthworms (*Lumbricus terrestris*). The specimen is placed in anesthesia (0.2% butanol in tap water) for 20 minutes. Then

it is pinned in a basin, ventral side facing upwards, and covered with preparation saline (0.04% butanol in saline, 26 mM $NaSO_4$ 25 mM NaCl, 6 mM $CaCl_2$, 4 mM KCl, 1 mM $MgCl_2$, 55 mM sucrose, 2 mM TRIS, adjusted to pH 7.4 (***Drewes and Pax, 1974***). The dissection starts with a small lateral incision caudally of the clitellum and it is followed by two longitudinal cuts alongside the VNC down to the posterior end. Afterwards the middle lappet is removed to lay open about 10 cm of the VNC. Gently pulling up the nerve chord reveals lateral connections which are then cut to disconnect the VNC from the rest of the nervous system. Once completely disconnected, the VNC is placed in chilled saline and kept at 4 °C for about 1 h.

Electrophysiological recording of colliding APs

We use a custom made nerve chamber made from Polyoxymethylene (***Figure 1*** bottom) which is encapsulated in a temperature controlled aluminum case (cover not shown in ***Figure 1***) and kept at 12 °C. It contains a row of silverchloride electrodes (diameter 0.8 mm), located 8 mm above the bottom of the chamber and separated by 5 mm from each other. The recording chamber is pre-filled with chilled saline. The isolated VNC is transferred to the chamber and the saline is drained, leaving the VNC resting on the electrodes. Finally, the chamber is sealed with a plastic sheet and the aluminum case is closed. Two stimulators (Grass SD-9) are connected to electrodes at the ends of the nerve. In between, three custom amplifiers connect the recording electrodes to a digital storage oscilloscope (LeCroy WaveRunner 6050). Triggering of stimulation and recording is done with an Arduino micro controller. Data is acquired with 1 MHz, smoothed with a savitzki-golay filter (width 51 µs) and baseline corrected with the asymmetric least squares method (***Eilers and Boelens, 2005***). The VNC contains two giant fibers, the median (MGF) and lateral giant fiber (LGF). These are unambiguously distinguished by their individual stimulation threshold and propagation velocity. For the analysis we used 3 collision sweep experiments. Each experiment consists of numerous recordings from 3 channels and varying delay, the complete data of experiment 3 is shown in ***Figure 1—figure Supplement 1***.

Models

General cable model for ephaptic coupling

The connection between inner electric potential V and transmembrane current is given by the general cable equation(***McNeal, 1976***; ***Rubinstein and Spelman, 1988***; ***Rattay, 1999***; ***Anastassiou et al., 2010***).

$$i_m = \frac{\partial I_{ax}}{\partial x} = \frac{1}{r_i}\left(\frac{\partial^2 V}{\partial x^2} + \frac{\partial V}{\partial x}\cdot\frac{\partial}{\partial x}\frac{1}{r_i}\right) \tag{5}$$

This equation describes both the generation of membrane current caused by an AP, and concomitant, the current induced by an external potential, as used in clinical applications (***Durand, 2014***; ***Merrill et al., 2005***; ***Tung, 2021***). In an infinite homogeneous neuron the membrane current is determined by the second derivative of the potential. The second term accounts for the spatial change of resistivity at any structural inhomogeneities, varicosities or neuron endings (***Basser and Roth, 2000***; ***Holt and Koch, 1999***). Assuming a constant capacity and neglecting external fields and inhomogeneities in the neuron one obtains the cable equation, eq. 1.

We assume the neurons being embedded in a large, homogeneous and isotropic conductor. In this case, the extracellular potential at a point r that is generated by the source neuron is given by

$$V_e(r) = \rho \int \mathrm{d}x \, \frac{i_m(x)}{|r - x|} \tag{6}$$

where ρ is the resistivity of the extracellular medium. The external potential $V_e(x,t)$ adds to the membrane potential $V_m(x,t)$ of the target neuron via $V = V_m + V_e$. Note that the target is considered to be in the resting state, where the transmembrane conductivity is negligible. The response is a redistribution of internal charges. In a static potential, the target neuron approaches a steady state by mirroring the external potential inhomogeneity in its transmembrane potential $V_m(x)$.

Relaxing Tasaki Model (RTM)

The repolarization of the extracellular potential missing in the TM model is added ad-hock by a repolarization function as follows. We introduce a state parameter n, which is 1 for the resting state. When the membrane voltage crosses the threshold value, n is set to 0 and its subsequent dynamic is given by

$$\dot{n}(t) = (1 - n(t))/\tau_r \,, \tag{7}$$

where τ_r is the repolarization time. The membrane parameters are controlled by

$$V_{eq} = -100\,\mathrm{mV}\, n^4 \quad \text{and} \quad g = g_m^\star (1 - n^4) \,. \tag{8}$$

For very large τ_r ($\gg \lambda^\star / v_p$), the RTM model reproduces the TM model, but eventually the resting state is restored a long time after an AP. With decreasing τ_r the repolarization affects the extracellular current and also the process of propagation. The exponent of n^4 effectively causes a delay of the repolarization. The values g and V_{eq} remain closer to the excited values for $t' < \tau_r/2$, where t' is the time since excitation. Under this condition the influence of the repolarization upon the initial rising phase is negligible. Consequently, the TM expressions for v_p and $\lambda^\star$ given above are in good agreement with the extended model (RTM).

Hodgkin Huxley (HH) model

The celebrated Hodgkin Huxley model also relies on the cable equation but adds a couple of additional equations to mimic the spatio-temporal shape of an AP (***Hodgkin and Huxley, 1952***). In particular, it incorporates the Nernst equilibrium and specific voltage and time dependent ionic conductances, resulting in a large number (typically of order 20!) of free parameters. This provides an enormous flexibility to account for almost any shape of AP. Nevertheless, our study reveals that the TM and RTM models which do not incorporate ion specific conductances are capable to fit experimental APs very well with only three degrees of freedom. We compare our data with the HH model for reference because of its widespread use and popularity. The complete equations and parameters are provided in ***Appendix 1***.

Simulations

Fitting to experiment

For simulations of the APs we use the three models introduced above (TM, RTM, HH), all with the same general parameters and morphology. The python module BRIAN (***Stimberg et al., 2019***) is used to simulate the nerve with a multi compartment model using a forth-order Runge-Kutta method with time steps of $0.1\,\mu\mathrm{s}$. After simulating the AP, the extracellular potential at the electrodes is calculated. In the nerve chamber, the nerve chord is hanging free between electrodes. The measuring electrode is surrounded by two ground electrodes which are $5\,\mathrm{mm}$ apart. All sections of the VNC that are in between the surrounding ground electrodes contribute to the measured potential according to

$$V_{el} = R_{el} \int_{-d}^{d} \mathrm{d}x\, i_m(x') \, \frac{d - x'}{2d} \,, \tag{9}$$

where x' is the distance to the point of contact with the recording electrode, d is the length of the freely hanging nerve between two neighboring electrodes and R_{el} is the resistance of the nerve chord between electrodes. We estimate the touching section of the nerve to be $0.8\,\mathrm{mm}$ (here $x' = 0$) and, accounting for the sagging of the nerve between electrodes, we integrate over $d = 5.2\,\mathrm{mm}$ in our calculations. In our approach, the magnitude of the TM model is controlled by $g_m^\star \cdot R_{el}$. For easier comparison, we first adjust the TM model to the magnitude of the HH model, which is achieved with $g_m^\star = 7.5\,\mathrm{mS/m}$. All parameters are presented in ***Appendix 2 — Table 2***.

Velocities are calculated from the time of AP arrival with an effective distance between the recording sites of $12\,\mathrm{mm}$. The width of the collision is measured by the full width at half maximum of the negative deflection of the extracellular potential, as shown in ***Figure 1—figure Supplement 2***.

The detailed settings as well as the calculated velocities and width are presented in ***Appendix 2 — Table 1***.

Predicted ephaptic coupling at synapses

We extended the standard BRIAN library to calculate the effect of an external field upon the target neuron by implementing eq. 5. The complete data for the end-shaft geometry with- and without bouton for all models is shown in ***Figure 4—figure Supplement 1***. Complete data for the end-end synapse is shown in ***Figure 4—figure Supplement 2***. We provide the full source code at osf.io/duyn3.

Acknowledgments

We thank Mahlon Kriebel, Georg Raiser, Sabine Kreissl, Shamit Shrivastava, Gerardo Alvarez for fruitful discussions. This work was supported by the Deutsche Forschungsgemeinschaft (DFG) in the frame of the R. Koselleck project Ma 817/9 as well as from the Zukunftskolleg Konstanz.

Data and materials availability

Source code and data have been deposited at the Center for Open Science (https://osf.io/duyn3/) Please refer to the readme file for further instructions.

References

Anastassiou CA, Koch C. Ephaptic Coupling to Endogenous Electric Field Activity: Why Bother? Curr Opin Neurobiol. 2015 Apr; 31:95–103. doi: 10.1016/j.conb.2014.09.002.

Anastassiou CA, Montgomery SM, Barahona M, Buzsáki G, Koch C. The Effect of Spatially Inhomogeneous Extracellular Electric Fields on Neurons. J Neurosci. 2010 Feb; 30(5):1925–1936. doi: 10.1523/JNEUROSCI.3635-09.2010.

Arvanitaki A. Effects Evoked in an Axon by the Activity of a Contiguous One. J Neurophysiol. 1942 Mar; 5(2):89–108. doi: 10.1152/jn.1942.5.2.89.

Baranauskas G, Martina M. Sodium Currents Activate without a Hodgkin and Huxley-Type Delay in Central Mammalian Neurons. J Neurosci. 2006 Jan; 26(2):671–684. doi: 10.1523/JNEUROSCI.2283-05.2006.

Barbour B. Only Negligible Deviations from Electroneutrality Are Expected in Dendritic Spines. Nat Rev Neurosci. 2020 Jan; 21(1):53–53. doi: 10.1038/s41583-019-0238-x.

Basser PJ, Roth BJ. New Currents in Electrical Stimulation of Excitable Tissues. Annu Rev Biomed Eng. 2000 Aug; 2(1):377–397. doi: 10.1146/annurev.bioeng.2.1.377.

Begum R, Bakiri Y, Volynski KE, Kullmann DM. Action Potential Broadening in a Presynaptic Channelopathy. Nat Commun. 2016 Jul; 7(1):12102. doi: 10.1038/ncomms12102.

Blot A, Barbour B. Ultra-Rapid Axon-Axon Ephaptic Inhibition of Cerebellar Purkinje Cells by the Pinceau. Nat Neurosci. 2014 Feb; 17(2):289–295. doi: 10.1038/nn.3624.

Catterall WA, Raman IM, Robinson HPC, Sejnowski TJ, Paulsen O. The Hodgkin-Huxley Heritage: From Channels to Circuits. J Neurosci. 2012 Oct; 32(41):14064–14073. doi: 10.1523/JNEUROSCI.3403-12.2012.

Chiang CC, Shivacharan RS, Wei X, Gonzalez-Reyes LE, Durand DM. Slow Periodic Activity in the Longitudinal Hippocampal Slice Can Self-Propagate Non-Synaptically by a Mechanism Consistent with Ephaptic Coupling. J Physiol. 2019; 597(1):249–269. doi: 10.1113/JP276904.

Cifra M. Electrodynamic Eigenmodes in Cellular Morphology. Biosystems. 2012 Sep; 109(3):356–366. doi: 10.1016/j.biosystems.2012.06.003.

Cole KS, Moore JW. Potassium Ion Current in the Squid Giant Axon: Dynamic Characteristic. Biophys J. 1960 Sep; 1(1):1–14. doi: 10.1016/S0006-3495(60)86871-3.

Debanne D, Campanac E, Bialowas A, Carlier E, Alcaraz G. Axon Physiology. Physiol Rev. 2011 Apr; 91(2):555–602. doi: 10.1152/physrev.00048.2009.

Drewes CD, Pax RA. Neuromuscular Physiology of the Longitudinal Muscle of the Earthworm, Lumbricus Terrestris: I. Effects of Different Physiological Salines. J Exp Biol. 1974 Apr; 60(2):445–452. doi: 10.1242/jeb.60.2.445.

Durand DM. Electrical Stimulation of Excitable Tissue. In: *Biomedical Engineering Fundamentals*, second ed. CRC Press; 2014.

Eccles JC. The Synapse: From Electrical to Chemical Transmission. Annu Rev Neurosci. 1982 Mar; 5(1):325–339. doi: 10.1146/annurev.ne.05.030182.001545.

Eilers PH, Boelens HF. Baseline Correction with Asymmetric Least Squares Smoothing. Leiden University Medical Centre Report. 2005; 1(1):5.

Fedosejevs CS, Schneider MF. Sharp, Localized Phase Transitions in Single Neuronal Cells. Proc Natl Acad Sci USA. 2022 Feb; 119(8). doi: 10.1073/pnas.2117521119.

Franken TP, Bondy BJ, Haimes DB, Goldwyn JH, Golding NL, Smith PH, Joris PX. Glycinergic Axonal Inhibition Subserves Acute Spatial Sensitivity to Sudden Increases in Sound Intensity. eLife. 2021 Jun; 10:e62183. doi: 10.7554/eLife.62183.

Funk RHW. Endogenous Electric Fields as Guiding Cue for Cell Migration. Front Physiol. 2015; 6.

Furukawa T, Furshpan EJ. Two Inhibitory Mechanisms in the Mauthner Neurons of Goldfish. J Neurophysiol. 1963 Jan; 26(1):140–176. doi: 10.1152/jn.1963.26.1.140.

Goldwyn JH, Rinzel J. Neuronal Coupling by Endogenous Electric Fields: Cable Theory and Applications to Coincidence Detector Neurons in the Auditory Brain Stem. J Neurophysiol. 2016 Jan; 115(4):2033–2051. doi: 10.1152/jn.00780.2015.

Hodgkin AL, Huxley AF. A Quantitative Description of Membrane Current and Its Application to Conduction and Excitation in Nerve. J Physiol. 1952 Aug; 117(4):500–544.

Holt GR, Koch C. Electrical Interactions via the Extracellular Potential Near Cell Bodies. J Comput Neurosci. 1999 Mar; 6(2):169–184. doi: 10.1023/A:1008832702585.

Horkay F, Tasaki I, Basser PJ. Osmotic Swelling of Polyacrylate Hydrogels in Physiological Salt Solutions. Biomacromolecules. 2000 Mar; 1(1):84–90. doi: 10.1021/bm9905031.

Iwakura A, Uchigashima M, Miyazaki T, Yamasaki M, Watanabe M. Lack of Molecular–Anatomical Evidence for GABAergic Influence on Axon Initial Segment of Cerebellar Purkinje Cells by the Pinceau Formation. J Neurosci. 2012 Jul; 32(27):9438–9448. doi: 10.1523/JNEUROSCI.1651-12.2012.

Jefferys JG. Nonsynaptic Modulation of Neuronal Activity in the Brain: Electric Currents and Extracellular Ions. Physiol Rev. 1995 Oct; 75(4):689–723. doi: 10.1152/physrev.1995.75.4.689.

Jeffress LA. A Place Theory of Sound Localization. J Comp Physiol Psychol. 1948 Feb; 41(1):35–39. doi: 10.1037/h0061495.

Katz B, Schmitt OH. Electric Interaction between Two Adjacent Nerve Fibres. J Physiol. 1940 Feb; 97(4):471–488.

Kléber AG, Rudy Y. Basic Mechanisms of Cardiac Impulse Propagation and Associated Arrhythmias. Physiol Rev. 2004 Apr; 84(2):431–488. doi: 10.1152/physrev.00025.2003.

Kole MJ, Qian J, Waase MP, Klassen TL, Chen TT, Augustine GJ, Noebels JL. Selective Loss of Presynaptic Potassium Channel Clusters at the Cerebellar Basket Cell Terminal Pinceau in Adam11 Mutants Reveals Their Role in Ephaptic Control of Purkinje Cell Firing. J Neurosci. 2015 Aug; 35(32):11433–11444. doi: 10.1523/JNEUROSCI.1346-15.2015.

Korn H, Faber DS. An Electrically Mediated Inhibition in Goldfish Medulla. J Neurophysiol. 1975 Mar; 38(2):452–471. doi: 10.1152/jn.1975.38.2.452.

Korn H, Faber DS. The Mauthner Cell Half a Century Later: A Neurobiological Model for Decision-Making? Neuron. 2005 Jul; 47(1):13–28. doi: 10.1016/j.neuron.2005.05.019.

Kriebel ME. Electrical Characteristics of Tunicate Heart Cell Membranes and Nexuses. J Gen Physiol. 1968 Jul; 52(1):46–59. doi: 10.1085/jgp.52.1.46.

Kriebel ME, Bennett MVL, Waxman SG, Pappas GD. Oculomotor Neurons in Fish: Electrotonic Coupling and Multiple Sites of Impulse Initiation. Science. 1969 Oct; 166(3904):520–524. doi: 10.1126/science.166.3904.520.

Levin M, Pezzulo G, Finkelstein JM. Endogenous Bioelectric Signaling Networks: Exploiting Voltage Gradients for Control of Growth and Form. Annu Rev Biomed Eng. 2017; 19(1):353–387. doi: 10.1146/annurev-bioeng-071114-040647.

Lyckman AW, Bittner GD. Axonal Conduction and Electrical Coupling in Regenerating Earthworm Giant Axons. Exp Neurol. 1992 Sep; 117(3):299–306. doi: 10.1016/0014-4886(92)90139-H.

Mateus JC, Lopes CDF, Aroso M, Costa AR, Gerós A, Meneses J, Faria P, Neto E, Lamghari M, Sousa MM, Aguiar P. Bidirectional Flow of Action Potentials in Axons Drives Activity Dynamics in Neuronal Cultures. J Neural Eng. 2021 Dec; 18(6):066045. doi: 10.1088/1741-2552/ac41db.

McCaig CD, Sangster L, Stewart R. Neurotrophins Enhance Electric Field-Directed Growth Cone Guidance and Directed Nerve Branching. Dev Dyn. 2000; 217(3):299–308. doi: 10.1002/(SICI)1097-0177(200003)217:3<299::AID-DVDY8>3.0.CO;2-G.

McNeal DR. Analysis of a Model for Excitation of Myelinated Nerve. IEEE Trans Biomed Eng. 1976 Jul; BME-23(4):329–337. doi: 10.1109/TBME.1976.324593.

Merrill DR, Bikson M, Jefferys JGR. Electrical Stimulation of Excitable Tissue: Design of Efficacious and Safe Protocols. J Neurosci Methods. 2005 Feb; 141(2):171–198. doi: 10.1016/j.jneumeth.2004.10.020.

Mussel M, Basser PJ, Horkay F. Ion-Induced Volume Transition in Gels and Its Role in Biology. Gels. 2021 Mar; 7(1):20. doi: 10.3390/gels7010020.

Naundorf B, Wolf F, Volgushev M. Unique Features of Action Potential Initiation in Cortical Neurons. Nature. 2006 Apr; 440(7087):1060–1063. doi: 10.1038/nature04610.

Plonsey R. Action Potential Sources and Their Volume Conductor Fields. P IEEE. 1977 May; 65(5):601–611. doi: 10.1109/PROC.1977.10539.

Pokorný J. Endogenous Electromagnetic Forces in Living Cells: Implications for Transfer of Reaction Components. Electro Magnetobiol. 2001 Jan; 20(1):59–73. doi: 10.1081/JBC-100103160.

Ramón y Cajal S. Histologie Du Système Nerveux de l'homme & Des Vertébrés. Ed. française rev. & mise à jour par l'auteur, tr. de l'espagnol par l. azoulay. ed. Paris: Maloine; 1909. doi: 10.5962/bhl.title.48637.

Rattay F. The Basic Mechanism for the Electrical Stimulation of the Nervous System. Neuroscience. 1999 Mar; 89(2):335–346. doi: 10.1016/S0306-4522(98)00330-3.

Rebollo B, Telenczuk B, Navarro-Guzman A, Destexhe A, Sanchez-Vives MV. Modulation of Intercolumnar Synchronization by Endogenous Electric Fields in Cerebral Cortex. Sci Adv. 2021 Mar; 7(10):eabc7772. doi: 10.1126/sciadv.abc7772.

Rubinstein JT, Spelman FA. Analytical Theory for Extracellular Electrical Stimulation of Nerve with Focal Electrodes. I. Passive Unmyelinated Axon. Biophys J. 1988 Dec; 54(6):975–981. doi: 10.1016/S0006-3495(88)83035-2.

Scott LL, Hage TA, Golding NL. Weak Action Potential Backpropagation Is Associated with High-Frequency Axonal Firing Capability in Principal Neurons of the Gerbil Medial Superior Olive. J Physiol. 2007; 583(2):647–661. doi: 10.1113/jphysiol.2007.136366.

Shivacharan RS, Chiang CC, Zhang M, Gonzalez-Reyes LE, Durand DM. Self-Propagating, Non-Synaptic Epileptiform Activity Recruits Neurons by Endogenous Electric Fields. Exp Neurol. 2019 Jul; 317:119–128. doi: 10.1016/j.expneurol.2019.02.005.

Shrivastava S. Detonation of Shock-Waves and Action Potentials in Lipid Interfaces. Proc Mtgs Acoust. 2018 Jul; 34(1):045034. doi: 10.1121/2.0000906.

Shrivastava S, Kang KH, Schneider MF. Collision and Annihilation of Nonlinear Sound Waves and Action Potentials in Interfaces. J R Soc Interface. 2018 Jun; 15(143):20170803. doi: 10.1098/rsif.2017.0803.

Siccardi S, Tuszynski JA, Adamatzky A. Boolean Gates on Actin Filaments. Phys Lett A. 2016 Jan; 380(1):88–97. doi: 10.1016/j.physleta.2015.09.024.

Southan AP, Robertson B. Patch-Clamp Recordings from Cerebellar Basket Cell Bodies and Their Presynaptic Terminals Reveal an Asymmetric Distribution of Voltage-Gated Potassium Channels. J Neurosci. 1998 Feb; 18(3):948–955. doi: 10.1523/JNEUROSCI.18-03-00948.1998.

Spach MS, Kootsey JM. Relating the Sodium Current and Conductance to the Shape of Transmembrane and Extracellular Potentials by Simulation: Effects of Propagation Boundaries. IEEE Trans Biomed Eng. 1985 Oct; BME-32(10):743–755. doi: 10.1109/TBME.1985.325489.

Spach Madison S , Barr Roger C , Serwer Gerald S , Johnson Edward A , Kootsey J Mailen. Collision of Excitation Waves in the Dog Purkinje System. Circ Res. 1971 Nov; 29(5):499–511. doi: 10.1161/01.RES.29.5.499.

Steinhaus BM, Spitzer KW, Isomura S. Action Potential Collision in Heart Tissue-Computer Simulations and Tissue Expenrments. IEEE Trans Biomed Eng. 1985 Oct; BME-32(10):731–742. doi: 10.1109/TBME.1985.325488.

Stimberg M, Brette R, Goodman DF. Brian 2, an Intuitive and Efficient Neural Simulator. eLife. 2019 Aug; 8:e47314. doi: 10.7554/eLife.47314.

Tasaki I. Collision of Two Nerve Impulses in the Nerve Fibre. Biochim Biophys Acta. 1949 Jan; 3:494–497. doi: 10.1016/0006-3002(49)90121-3.

Tasaki I. New Measurements of the Capacity and the Resistance of the Myelin Sheath and the Nodal Membrane of the Isolated Frog Nerve Fiber. Am J Physiol. 1955 Jun; 181(3):639–650.

Tasaki I. Spread of Discrete Structural Changes in Synthetic Polyanionic Gel: A Model of Propagation of a Nerve Impulse. J Theor Biol. 2002 Oct; 218(4):497–505. doi: 10.1006/jtbi.2002.3095.

Tasaki I. A Note on the Local Current Associated with the Rising Phase of a Propagating Impulse in Nonmyelinated Nerve Fibers. Bull Math Biol. 2006 Apr; 68(2):483. doi: 10.1007/s11538-005-9012-5.

Tasaki I. Physiology and Electrochemistry of Nerve Fibers. Elsevier; 2012.

Tasaki I, Singer I, Watanabe A. Excitation of Internally Perfused Squid Giant Axons in Sodium-Free Media. Proc Natl Acad Sci USA. 1965 Sep; 54(3):763–769. doi: 10.1073/pnas.54.3.763.

Tasaki I, Watanabe A, Hallett M. Properties of Squid Axon Membrane as Revealed by a Hydrophobic Probe, 2-p-Toluidinylnaphthalene-6-Sulfonate. Proc Natl Acad Sci USA. 1971 May; 68(5):938–941. doi: 10.1073/pnas.68.5.938.

Tasaki I, Matsumoto G. On the Cable Theory of Nerve Conduction. Bull Math Biol. 2002 Nov; 64(6):1069. doi: 10.1006/bulm.2002.0310.

Treue S. Attentional Selection: Mexican Hats Everywhere. Curr Biol. 2014 Sep; 24(18):R838–R839. doi: 10.1016/j.cub.2014.08.019.

Tung L. The Generalized Activating Function. In: Efimov IR, Ng FS, Laughner JI, editors. *Cardiac Bioelectric Therapy: Mechanisms and Practical Implications* Cham: Springer International Publishing; 2021.p. 77–89. doi: 10.1007/978-3-030-63355-4_7.

Weiss SA, Preuss T, Faber DS. A Role of Electrical Inhibition in Sensorimotor Integration. Proc Natl Acad Sci USA. 2008 Nov; 105(46):18047–18052. doi: 10.1073/pnas.0806145105.

Appendix 1

HH model

The HH model (***Hodgkin and Huxley, 1952***) is implemented using standard parameters and expressions. We use the source code based on an example provided with the brian package (https://brian2.readthedocs.io/en/stable/examples/compartmental.hodgkin_huxley_1952.html, ***Stimberg et al.*** (***2019***).) The total resistive current is given by

$$i_r = g_l(E_l - v) + g_{Na} m^3 h(E_{Na} - v) + g_K n^4 (E_K - v)\,,$$

These three terms (channels) drive the membrane towards specific equilibrium values

$$E_{Na} = 115\,\mathrm{mV}\,, \quad E_K = -12\,\mathrm{mV}\,, \quad E_l = 10.6\,\mathrm{mV}\,.$$

The conductivities g_{Na}, g_K, g_l are controlled by

$$g_{Na} = 1200\,\mathrm{S/m^2}\,, \quad g_K = 360\,\mathrm{S/m^2}\,, \quad g_l = 3\,\mathrm{S/m^2}$$

and

$$\frac{\mathrm{d}m}{\mathrm{d}t} = \alpha_m(1-m) - \beta_m m\,, \quad \frac{\mathrm{d}n}{\mathrm{d}t} = \alpha_n(1-n) - \beta_n n\,, \quad \frac{\mathrm{d}h}{\mathrm{d}t} = \alpha_h(1-h) - \beta_h h\,,$$

with

$$\alpha_m = 1\,\mathrm{kHz}/\mathrm{exprel}\left(\frac{-v + 25\,\mathrm{mV}}{10\,\mathrm{mV}}\right)$$

$$\beta_m = 4\,\mathrm{kHz}\ \exp(-v/18\,\mathrm{mV})$$

$$\alpha_h = 70\,\mathrm{kHz}\ \exp(-v/20\,\mathrm{mV})$$

$$\beta_h = 1\,\mathrm{kHz}/\exp\left(\frac{-v + 30\,\mathrm{mV}}{10\,\mathrm{mV}}\right)$$

$$\alpha_n = 100\,\mathrm{Hz}/\mathrm{exprel}\left(\frac{-v + 25\,\mathrm{mV}}{10\,\mathrm{mV}}\right)$$

$$\beta_n = 125\,\mathrm{Hz}\ \exp(-v/80\,\mathrm{mV})$$

To avoid singularities, this implementation uses the function exprel which is provided by BRIAN (***Stimberg et al., 2019***) , and is defined as

$$\mathrm{exprel}(x) = \begin{cases} 1, & \text{if } x = 0 \\ \frac{\exp(x)-1}{x}, & \text{otherwise} \end{cases}$$

Appendix 2

Additional experimental results

	exp. 1	exp. 2	exp. 3	(unit)
# recordings	21	21	46	
delay range	4	4.5	4.5	ms
delay step	0.2	0.23	0.1	ms
sampling rate	1	1	1	MHz
duration	10	10	10	ms
v_p C1→C2	16.2	16.2	16.3	m/s
v_p C1→C2	15.0	15.2	16.2	m/s
v_p C1←C2	15.1	15.1	14.9	m/s
v_p C1←C2	15.0	15.1	14.9	m/s
v_p C2→C3	13.1	13.1	13.3	m/s
v_p C2→C3	13.2	13.1	13.4	m/s
v_p C2←C3	13.0	14.3	14.5	m/s
v_p C2←C3	13.1	14.6	14.8	m/s
width	10.2	9.9	8.7	mm

Appendix 2—table 1. Experiment details Settings as well as measured velocity and width of each experiment.

Model	r_i (MΩ/m)	c_m (mF/m)	$r_i c_m$ (s/m^2)	$g^\star$ (mS/m)	v_p (m/s)	$\lambda^\star$ (mm)	amp.
TM	2.6	9.94	26	113.1	14.9	1.8	1.00
HH	61.5	0.46	28	-	-	-	0.07
TM_{HH}	39.8	0.65	26	7.5	14.9	1.8	0.07
RTM_{HH}	75.3	0.47	36	7.5	15.0	1.3	0.04

Appendix 2—table 2. Model parameters The results from the fitting procedure are r_i and c_m, these values depend on the model that is used. For the model termed TM_{HH} we adjusted the amplitude (amp.) of the TM model to match the HH model by choosing an appropriate $g^\star$. This lower value of $g^\star$ is also used for the RTM model. Internally the simulation uses a diameter of $80\,\mu m$, The rows v_p and $\lambda^\star$ contain the result of the analytical expressions of the TM model. The expressions for v_p and $\lambda^\star$ are coarse approximations for the RTM model, but do not apply to the HH model.

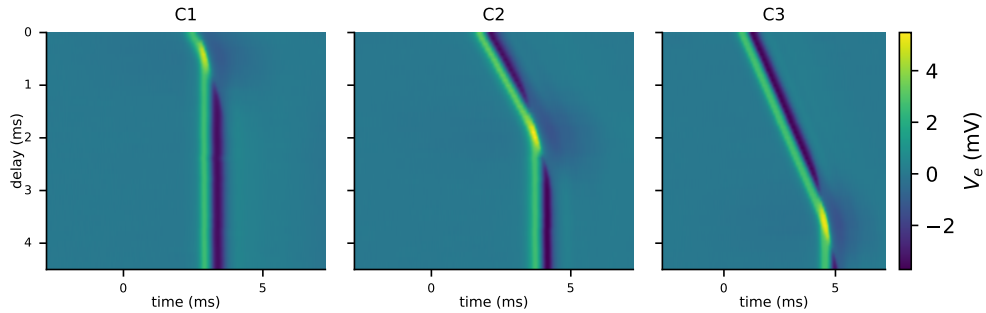

Figure 1—figure supplement 1. Complete raw data from experiment number 3 (out of 3).

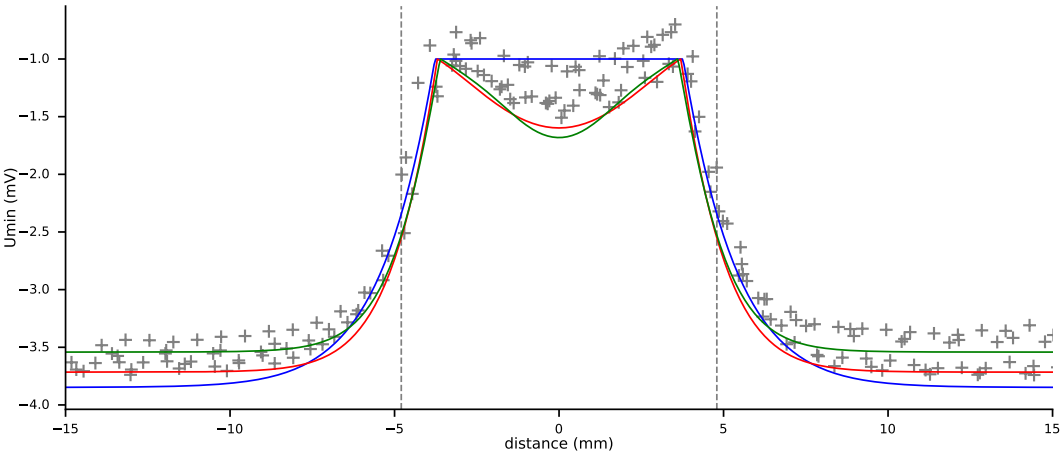

Figure 1—figure supplement 2. Grey crosses show the maximal negative deflection of the extracellular potential from 88 recordings (C1, C2, C3 from 3 experiments). Grey dashed lines denote the Full width at half maximum (from channel C2 from all 3 experiments), which is used to fit the models. Continuous lines are the TM model (blue), RTM model (red) and HH model (green). For better comparison, the simulated curves are shifted to peak at $-1\,\mathrm{mV}$.

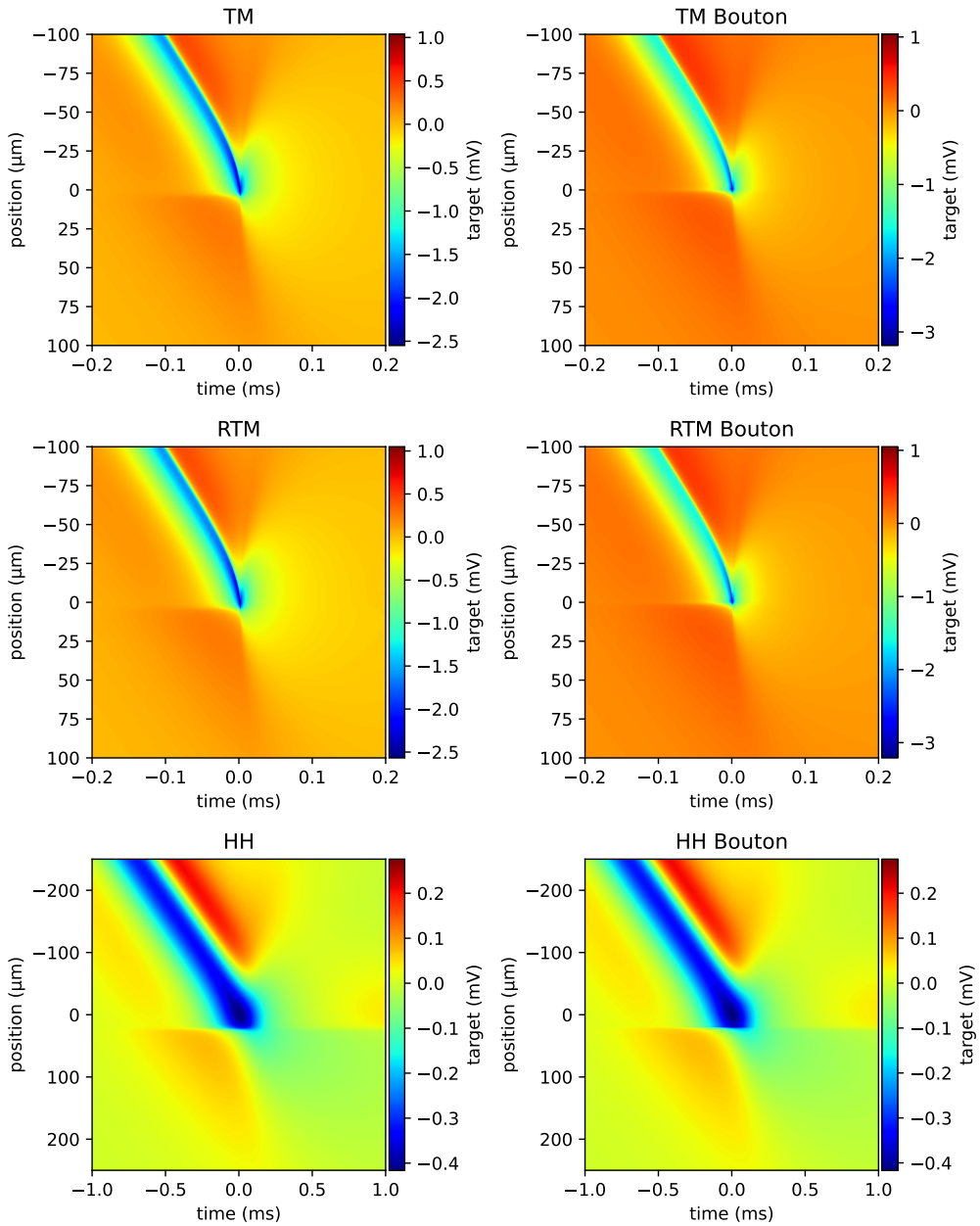

Figure 4—figure supplement 1. Simulation of target potential in an end-shaft synapse The y-axis denotes the position along the target where $y = 0$ refers to the target position next to the end of the source axon terminal.

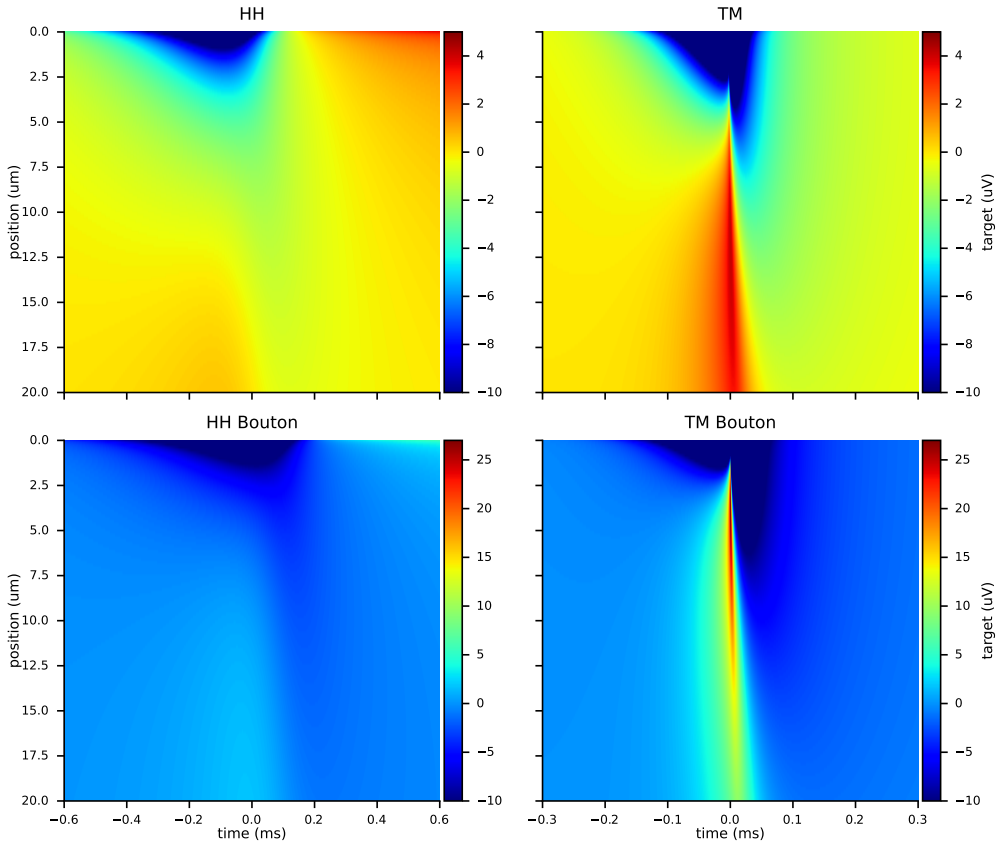

Figure 4—figure supplement 2. Simulation of target potential in an end-end synapse The y-axis denotes the position along the target where $y = 0$ refers to the tip of the target at the synaptic gap. The color scale is cropped at $-10\,\mu\mathrm{V}$.